

II. Physics of Optical Parametric Oscillator Network

This chapter describes the physics of the optical parametric oscillator (OPO) and OPO network, a key component in the quantum neural network (QNN). The OPO is based on a second-order ($\chi^{(2)}$) optical nonlinearity in non-centrosymmetric crystals, which allows photons of a pump frequency to be down-converted into pairs of photons at the half-harmonic [1]. Such a phenomenon allows for phase-sensitive amplification and oscillation: below a threshold pump power, the system lives in a squeezed vacuum state, while above threshold, it can oscillate in one of two (coherent) phase states. This bifurcation provides the computational mechanism for the Ising machine: a network of OPOs can be driven from below to above threshold, while the optical coupling encodes the Ising problem and allows the system to search for the Ising ground state.

2.1 Parametric amplification

In a non-centrosymmetric crystal like LiNbO₃ or BBO [2], the optical polarization depends on both the first and second powers of the electric field:

$$P_i = \underbrace{\sum_j \chi_{ij}^{(1)} E_j}_{P^{(1)}} + \underbrace{\sum_k \chi_{ijk}^{(2)} E_j E_k}_{P^{(2)}}. \quad (1)$$

One can drive the Maxwell's Equations by the linear and nonlinear polarizations, Eq.(1), to derive a set of *nonlinear* equations for electromagnetic wave propagation. Because the equations are nonlinear to second order, they permit three-wave mixing phenomena $E(\omega_1) + E(\omega_2) \leftrightarrow E(\omega_1 + \omega_2)$ - for example, second-harmonic generation, sum frequency generation, difference frequency generation, and parametric amplification. This is in contrast to linear optics, where waves of different frequencies do not mix.

Optical nonlinearities are weak enough that we can assume $P^{(2)} \ll P^{(1)}$ and solve these equations perturbatively. Of many possible nonlinear processes, the dominant one is chosen by the phase-matching condition $k_1 + k_2 - k_3 = \pm 2\pi/\Lambda$, where $k_{1,2,3}$ are the wave vectors of the three frequencies and Λ is a poling period of the nonlinear crystal (if any). It is usually difficult to simultaneously satisfy phase-matching and energy conservation ($\omega_1 + \omega_2 - \omega_3 = 0$) conditions. Nonlinear crystals must be engineered to activate a particular

nonlinear process. For degenerate parametric amplification (the process relevant to the QNN), Maxwell's equations reduce to: $\frac{da}{dz} = \epsilon ba^*$:

$$\frac{da}{dz} = \epsilon ba^* \quad (2)$$

$$\frac{db}{dz} = -\frac{1}{2}\epsilon a^2. \quad (3)$$

In Eqs.(2, 3) there are two fields: a pump $b(z)$ at frequency 2ω and a signal $a(z)$ at frequency ω . These are normalized to photon flux: the pump and signal power are $P_b = 2\hbar\omega|b|^2$ and $P_a = \hbar\omega|a|^2$, respectively, while $\epsilon = (\hbar\omega^3/\epsilon_0c^3n^3A_{\text{eff}})^{1/2}\chi_{\text{eff}}^{(2)}$. Here A_{eff} is a cross-sectional area of the two beams [2].

If we start with a strong pump ($b > 0$) and a weak signal, the signal will be amplified according to Eq.(2). Since da/dz scales with a^* rather than a , this is *phase-sensitive* amplification in which the real part is amplified while the imaginary part is de-amplified. If the signal is sufficiently weak, back-conversion to the pump (Eq.(3)) is negligible and the signal grows exponentially:

$$\text{Re}[a(z)] = e^{\epsilon bz}\text{Re}[a(0)], \quad \text{Im}[a(z)] = e^{-\epsilon bz}\text{Im}[a(0)]. \quad (4)$$

Accounting for back-conversion, we see that the quantity $B^2 = |b|^2 + \frac{1}{2}|a|^2$ must be conserved. If both of the fields are real, the solution takes the form

$$a(z) = \sqrt{2}B \text{sech}(\epsilon B(z - z_0)), \quad b(z) = -B \tanh(\epsilon B(z - z_0)), \quad (5)$$

which is plotted in Fig. 1.

To calculate the OPA gain, we use the initial conditions $(a_{\text{in}}, b_{\text{in}})$ to calculate the two parameters (B, z_0) using solution Eq.(5) at $z = 0$. Then we propagate to the end of the crystal and compute $a_{\text{out}} = a(z = L)$. The overall input-output relation may be written as

$$a_{\text{out}} = a_{\text{in}} G_0^{\frac{1}{2}} \sqrt{(b_{\text{in}}^2 + a_{\text{in}}^2/2)/b_0} \left[1 + (G_0^{\sqrt{(b_{\text{in}}^2 + a_{\text{in}}^2/2)/b_0}} - 1) \frac{1 - \sqrt{b_{\text{in}}^2/(b_{\text{in}}^2 + a_{\text{in}}^2/2)}}{2} \right]^{-1}. \quad (6)$$

Here G_0 is defined as the cavity loss rate or *threshold gain* of the parametric oscillator -- the

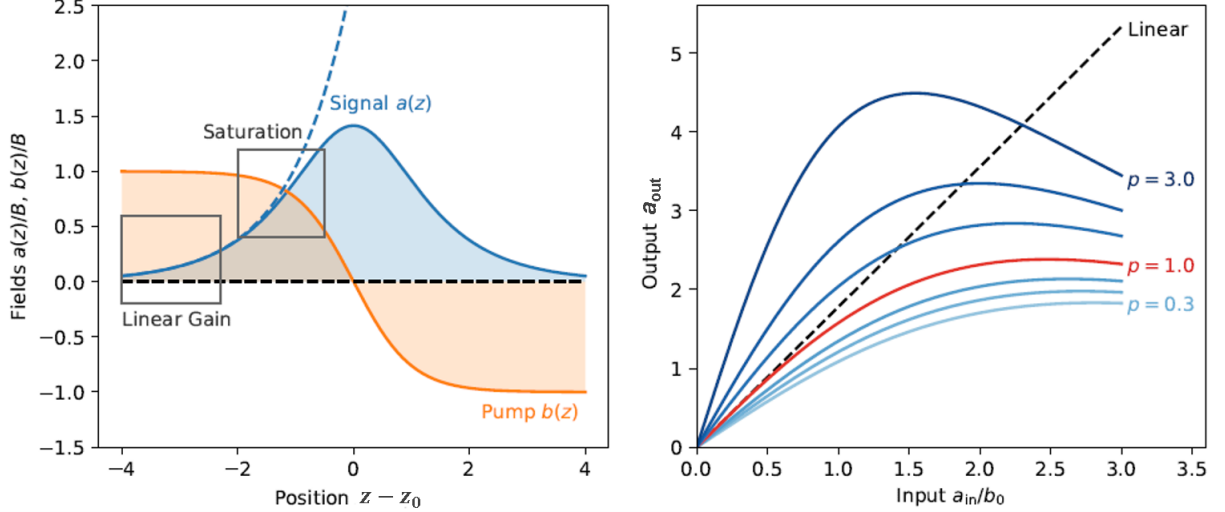


FIG. 1: Left: pump and signal fields as a function of propagation distance, Eq.(5), with regions of linear gain and gain saturation shown. Right: Input-output relation ($G_0 = 5$ dB), as a function of normalized pump amplitude $p = b_{\text{in}}/b_0$, showing saturation due to pump depletion.

gain required to offset cavity loss. Since power gain goes as $e^{2\epsilon bL}$ for weak signals (Eq.(4)), we defined the threshold pump as $b_0 = (2\epsilon L)^{-1} \log(G_0)$. The key parameter is the pump amplitude normalized to the threshold: $p = b_{\text{in}}/b_0$. The input-output relation is plotted in Fig. 1.

Eq.(6) has two limits:

1. $a_{\text{in}} \ll b_{\text{in}}$: In this case, we have linear gain: $a_{\text{out}} \approx G_0^{p/2} a_{\text{in}}$.
2. $a_{\text{in}} \gg b_{\text{in}}$: The signal is much stronger than the pump, so the parametric process is inverted. Instead of parametric gain, we have second-harmonic generation, which depletes the signal. The depletion increases with power: $a_{\text{out}} = 2G_0^{-2-3/2 a_{\text{in}}/b_0} a_{\text{in}}$.

For the QNN, we are typically interested in the near-threshold behavior at $p \approx 1$, where the computation happens. In this limit, we have linear gain $G_0^p \approx G_0(1 + \frac{1}{2}(p-1) \log G_0)$ and a saturation term obtained by expanding Eq.(6) to third order in a_{in} :

$$a_{\text{out}} = G_0 \left[1 + \underbrace{\frac{\log(G_0)}{2}(p-1)}_{\text{gain}} - \underbrace{\frac{G_0 - (1 + \log G_0)}{8}(a_{\text{in}}/b_0)^2}_{\text{saturation}} \right] a_{\text{in}}. \quad (7)$$

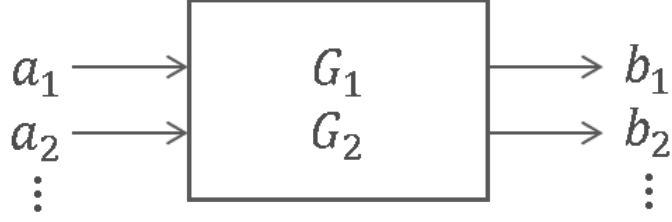


FIG. 2: Two quadrature components of E-field .

2.2 General quantum limit of linear amplifiers

In a linear amplifier shown in Fig. 2, the two quadrature components, $\hat{a}_1 = \frac{1}{2} (\hat{a} + \hat{a}^\dagger)$ and $\hat{a}_2 = \frac{1}{2i} (\hat{a} - \hat{a}^\dagger)$, are amplified with different gain coefficients and added with different noise terms:

$$\begin{aligned}\hat{b}_1 &= \sqrt{G_1} \hat{a}_1 + \hat{F}_1 \\ \hat{b}_2 &= \sqrt{G_2} \hat{a}_2 + \hat{F}_2.\end{aligned}\tag{8}$$

We impose the bosonic commutation relation not only for the input signal but also for the output signal

$$[\hat{a}, \hat{a}^\dagger] = [\hat{b}, \hat{b}^\dagger] = 1,\tag{9}$$

or

$$[\hat{a}_1, \hat{a}_2] = [\hat{b}_1, \hat{b}_2] = \frac{i}{2}.\tag{10}$$

If we substitute the input-output relation Eq. (8) into the commutation relation Eq. (10), we obtain

$$\begin{aligned}[\hat{b}_1, \hat{b}_2] &= [\sqrt{G_1} \hat{a}_1 + \hat{F}_1, \sqrt{G_2} \hat{a}_2 + \hat{F}_2] \\ &= \sqrt{G_1 G_2} [\hat{a}_1, \hat{a}_2] + [\hat{F}_1, \hat{F}_2],\end{aligned}\tag{11}$$

where we use the fact that the input signal and internal noise operators commute. Using Eq. (10) in Eq. (11), we obtain

$$\left[\hat{F}_1, \hat{F}_2\right] = \left(1 - \sqrt{G_1 G_2}\right) \frac{i}{2}. \quad (12)$$

Therefore, if a particular amplifier satisfies $G_1 G_2 = 1$, the commutator bracket $\left[\hat{F}_1, \hat{F}_2\right]$ is equal to zero, which means such a phase sensitive amplifier with $G_1 = 1/G_2 \gg 1$ does not need to add extra noise to the amplified and deamplified outputs. On the other hand, a phase insensitive amplifier with $G_1 = G_2 \gg 1$ must add the extra noise, $\langle \Delta \hat{F}_1^2 \rangle = \langle \Delta \hat{F}_2^2 \rangle = \frac{G^2}{4}$, to the amplified outputs.

This is the general quantum limit of linear amplifiers [3], which is considered as a special case of the generalized Heisenberg uncertainty product for simultaneous measurements of two conjugate observables [4]. That is, if one tries to measure (or amplify) the two conjugate observables simultaneously, such a measurement (or amplification) must accompany the addition noise of a measuring device in addition to the intrinsic noise of a measured object. As a result of this extra noise, the uncertainty product is doubled from the Heisenberg limit.

The degenerate optical parametric amplifier (DOPA) enhances the in-phase component \hat{a}_1 for information readout but suppresses the quadrature-phase component \hat{a}_2 to discard this information. In this way, the DOPA escapes from the extra noise.

2.3 Supercritical pitchfork bifurcation

To construct a single OPO, we place the OPA element discussed above inside a cavity. The round-trip cavity loss is G_0^{-1} , while the phase-sensitive gain is governed by Eq.(7). The field amplitude a does not change much between two round trips, so the resulting difference equation can be converted into a differential equation:

$$\frac{da}{dt} = \left[\frac{\log(G_0)}{2}(p-1) - \frac{G_0 - (1 + \log G_0)}{8}(a/b_0)^2 \right] a \equiv \frac{\partial V(a)}{\partial a}, \quad (13)$$

where $V(a)$ is the effective potential for the OPO field a . Figure 3 shows the change of the effective potential $V(a)$ and the OPO wavefunction as a function of the normalized pump rate p . For $p < 1$ (below threshold) this has only one steady state: $a = 0$. This is the classical limit of the squeezed vacuum state that exists in a below-threshold OPO. Above threshold, the state $a = 0$ is unstable and there are two stable steady-states:

$$a = \pm b_0 \sqrt{\frac{4 \log(G_0)}{G_0 - (1 + \log G_0)} (p - 1)}. \quad (14)$$

These states are the classical limit of the binary coherent states of an above-threshold OPO. Many physical systems feature a similar behavior, supercritical Pitchfork bifurcation, at a critical point.

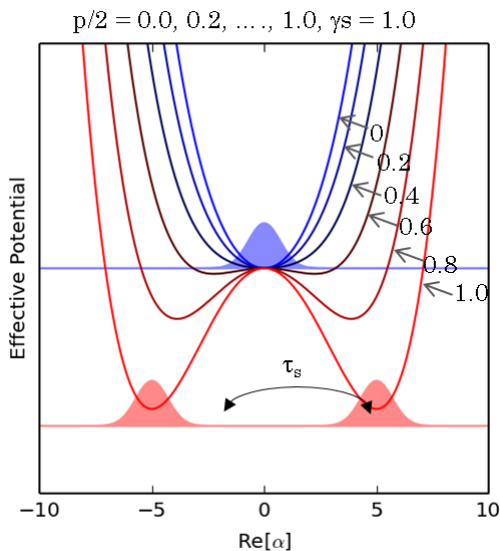


FIG. 3: Change of the effective potential $V(a)$ and the OPO wavefunction as a function of the normalized pump rate p .

2.4 OPO network

Our implementation of the QNN realizes N OPOs in a single cavity by *time-multiplexing*: a single OPO corresponds to an intra-cavity pulse which is synchronously pumped with a pulsed laser with repetition rate N times the cavity free spectral range [5]. Each OPO pulse in the cavity corresponds to an independent OPO. The nonlinear dynamics can add additional degrees of freedom to each OPO pulse, which can cause unusual dynamics at high pump powers; however, near threshold they are well described by our model [6].

The Ising potential $J_{ij}\sigma_i\sigma_j$ is realized *dissipatively* through coupling of the OPOs, in contrast to quantum annealing and high-Q OPO qubits, where the potential is always conservative, i.e. Hamiltonian [8, 9]. This makes the Ising machine fundamentally different from these other approaches. To couple the OPOs (realized as pulses multiplexed in time),

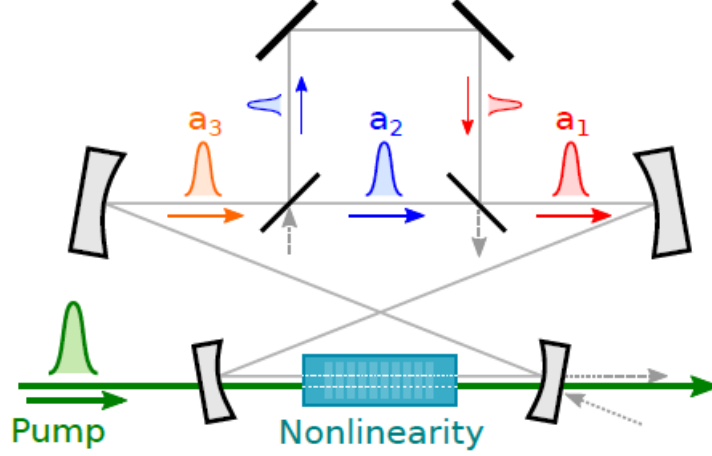


FIG. 4: Time-multiplexed implementation using delay lines for couplings [7].

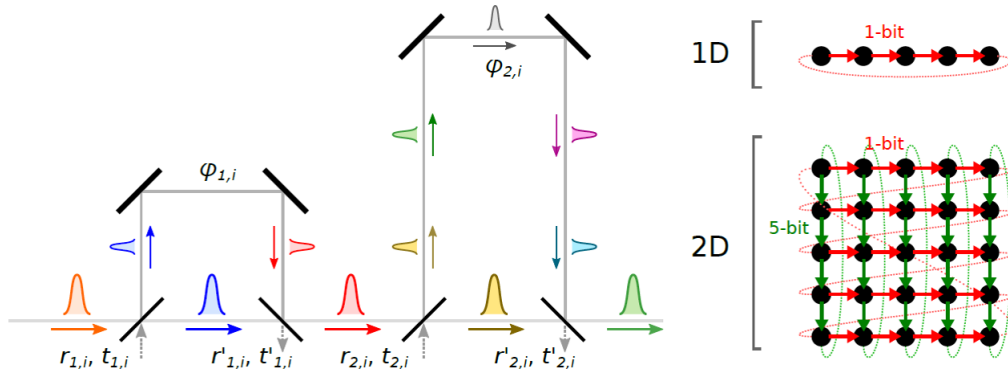


FIG. 5: Left: 1-bit and 4-bit delay line couplings. Right: Ising lattices realized with a single coupling (top) and two couplings (bottom) [7].

one needs some way to delay the pulses and re-insert them at later times as shown in Fig. 4. An array of *delay lines* (Fig. 5) is one way to implement a complicated Ising coupling matrix. A single d -bit delay realizes the interaction:

$$a_i \rightarrow t^2 a_i + r^2 a_{i-d}, \quad (15)$$

where (t, r) are the (potentially time-dependent) mirror transmission/reflection coefficients. Any optical coupling can be built up from $n - 1$ delay lines, provided the lines have time-dependent amplitude and phase modulators [10]. If the couplings r are small enough, the delay lines commute so their order does not matter, and the effect on the equations of motion is:

$$\frac{da_i}{dt} = \left[\underbrace{\frac{\log(G_0)}{2}(p-1)}_{\text{gain}} - \underbrace{\frac{G_0 - (1 + \log G_0)}{8}(a_i/b_0)^2}_{\text{saturation}} \right] a_i + \underbrace{\sum_d r_d^2 (a_{i-d} - a_i)}_{\text{coupling/loss}}. \quad (16)$$

By scaling t to the photon lifetime, we put (Eq. (16)) into a standard form:

$$\boxed{\frac{da_i}{dt} = [(p-1) - \beta a_i^2] a_i + \eta \sum_j J_{ij} a_j}, \quad (17)$$

where β is the saturation parameter, J_{ij} is the Ising coupling matrix, and η is the coupling strength, given by:

$$\beta = \frac{G_0 - (1 + \log G_0)}{4b_0^2 \log(G_0)}, \quad \eta J_{ij} = \sum_d r_d^2 (\delta_{i-d,j} - \delta_{i,j}). \quad (18)$$

2.5 Example: Ising spins on cubic graph

Figure 6 illustrates the experimental setup, in which $N = 4$ OPO pulses in a free-space ring cavity are coupled by three optical delay lines [5]. The optical delay line with a one-bit delay implements a clock-wise directional Ising coupling, while those with a two-bit delay and three-bit delay implement a diagonal unidirectional coupling and counter-clock-wise directional coupling. Each OPO pulse is connected to three other OPO pulses (cubic graph), and the corresponding graph is a complete graph in this case.

The sequential measurement results by a one-bit delay differential detector and corresponding phase patterns (or Ising spin configurations) are shown in Fig. 7(a). The total number of $2^4 = 16$ Ising spin configurations are split into the four sequential measurement patterns. Fig. 7(b) compares the measurement statistics over 1,000 runs for the two cases: Ising coupling is off and on [5]. All Ising couplings are anti-ferromagnetic, i.e. $J_{ij} = -1$. When the Ising coupling is off, each OPO selects 0-phase or π -phase independently and randomly, so that eight degenerate configurations are observed with identical probabilities. However, when the Ising coupling is on, only three degenerate ground states are observed with equal probabilities and five excited states are not observed at all.

Figure 8 (a) illustrates the experimental setup, in which $N = 16$ OPO pulses in a free-space ring cavity are coupled by three optical delay lines [11]. The optical delay line with

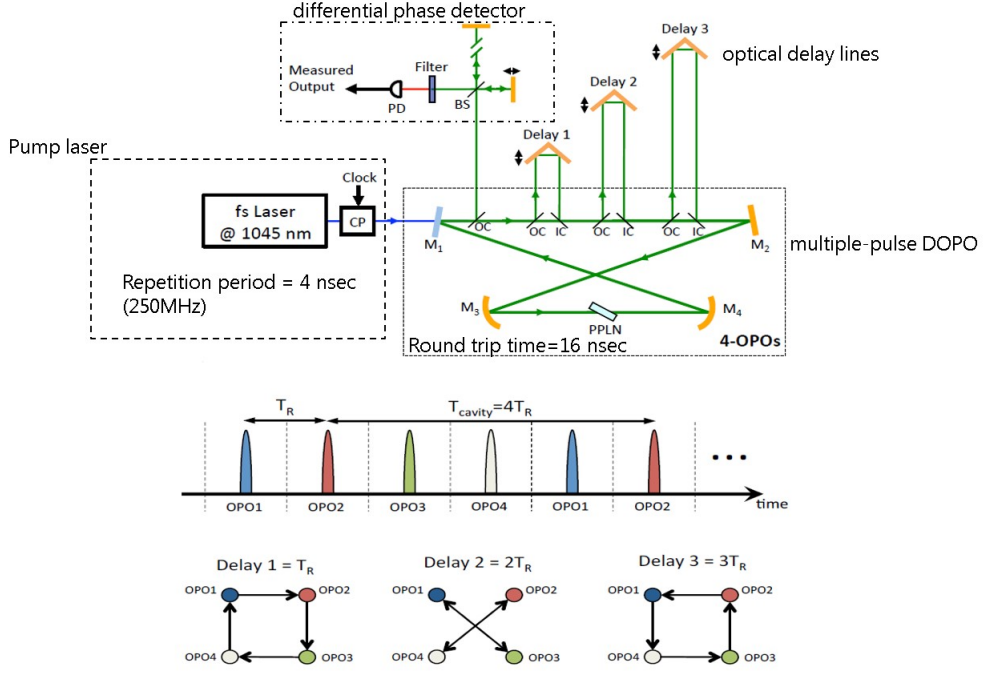


FIG. 6: Implementation of $N = 4$ Ising machines with free-space OPO [5].

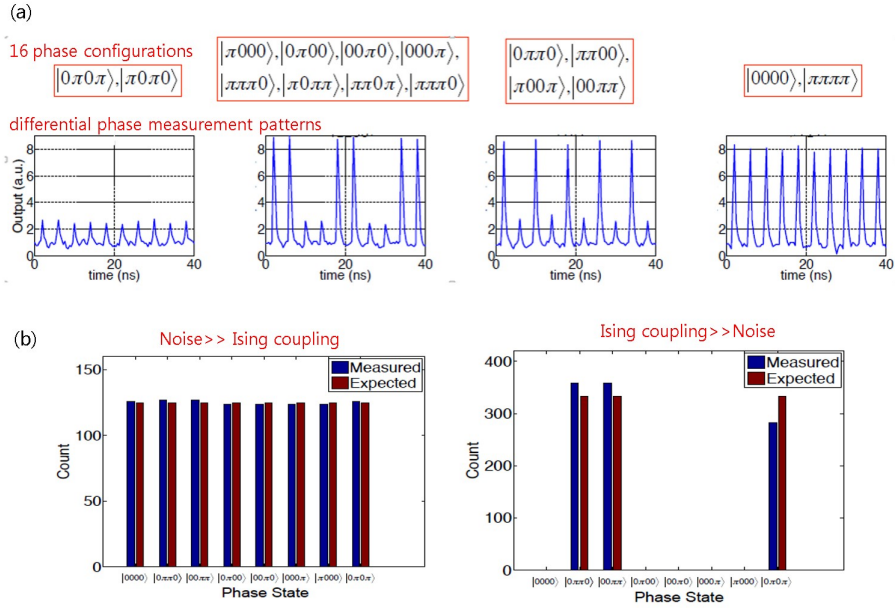


FIG. 7: NP-hard MAX-CUT-3 Problem: Experimental Results. (a) Four differential phase measurement patterns. (b) Measurement statistics for the case of Ising coupling off and on [5].

a one-bit delay implements a directional clock-wise nearest neighbor coupling, while the optical delay lines with an eight-bit delay and fifteen-bit delay implement an undirectional diagonal coupling and directional counter-clock-wise nearest neighbor coupling, as shown in Fig. 8(b). The implemented graph is a Möbius-Ladder graph on cubic graph. The three

representative differential phase detection outputs in this setup are shown in Fig. 9, in which a ferromagnetic phase, anti-ferromagnetic phase and the ground state of a Möbius-Ladder graph with anti-ferromagnetic couplings. Only sixteen degenerate ground states are observed and any excited states of $\sim 10^5$ are not observed over 2,000 runs as shown in Table I.

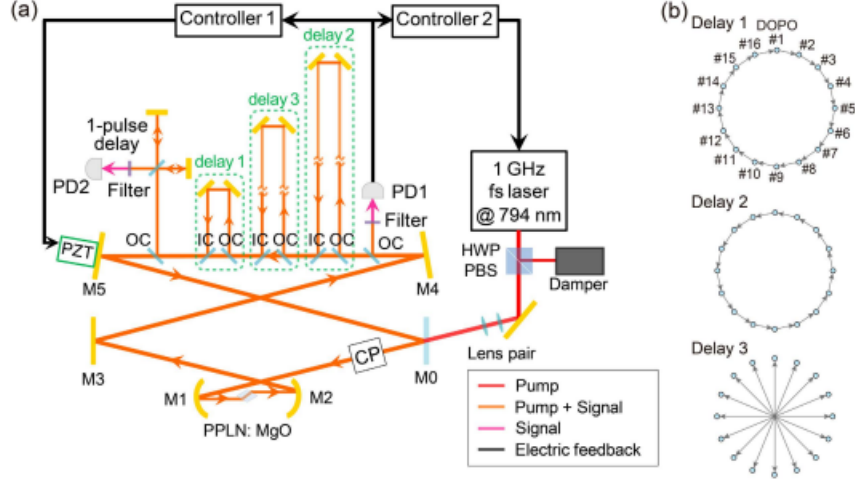


FIG. 8: Experimental setup. (a) The pump laser is a Ti:sapphire femtosecond pulse laser with a central wavelength of 794 nm. The OPO ring cavity is 4.8 m long, and the round trip time for the pulses is 16 ns. Three delay lines implement the optical coupling between the DOPO pulses. An unequal-arm Michelson interferometer measures the relative phases of adjacent signal pulses. Two servo controllers are used to stabilize the OPO under the operation of the mechanical chopper. (b) Couplings introduced by each optical delay line. Delay 1 (1 ns) couples adjacent pulses in the forward direction, while that of Delay 2 (15 ns) is backward, feeding the pulses back to those of the next round trip. Delay 3 (8 ns) introduces the mutual couplings between the pulses which are half round trip (8 pulses) away. HWP: half wave plate, PBS: polarizing beamsplitter, CP: chopper, M: mirror, IC: input coupler, OC: output coupler, PD: photodetector, PZT: piezoelectric transducer [11].

2.6 Example: 1D Ising spin chains

As a model system, we consider the 1D Ising chain. Realizing this in the Ising machine is particularly simple: only a single or two delay lines are needed [7, 12]. Since 1D systems have been studied extensively in classical statistical mechanics, this gives us a wide body of literature to compare against.

The evolution of the 1D chain is a two-stage process: in the *growth stage*, the field is weak compared to the saturation value, pump depletion can be ignored and the signal grows exponentially from the vacuum. Because of inter-pulse coupling, different (Fourier) modes

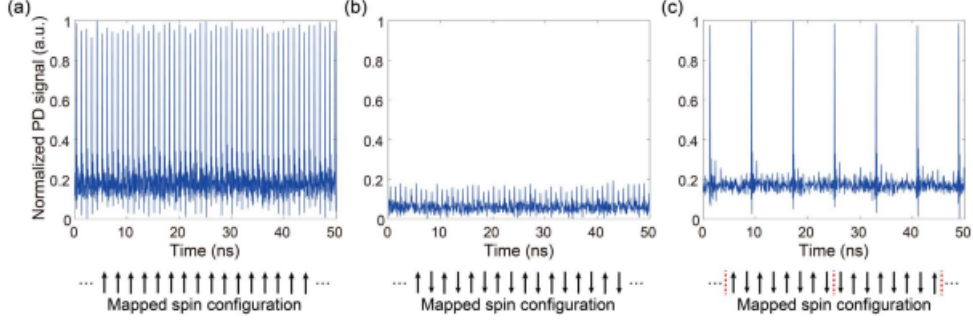


FIG. 9: Interferometer output signals corresponding to the ground states. (a) Complete same-phase order for the one-dimensional ferromagnetic ring instance. (b) Complete alternating-phase order for the one-dimensional anti-ferromagnetic ring instance. (c) Answer to MAX-CUT; Two alternating-phase (antiferromagnetic) domains containing eight pulses, with frustration at the boundaries for a cubic-graph instance. Corresponding Ising spin configuration is shown below each graph. Red dashed lines in (c) display the domain boundaries [11].

TABLE I: Summary of the performance of the 4-bit and 16-bit coherent Ising machine [11].

	One-dimensional ring, ferromagnetic	One-dimensional ring, anti-ferromagnetic	Cubic graph, anti-ferromagnetic ($N = 16$)
Coupling	$J_{i,i+1} = J_{i+1,i} = 1$ (delay 1, 2)	$J_{i,i+1} = J_{i+1,i} = -1$ (delay 1, 2)	$J_{i,i+1} = J_{i+1,i} = -1$ $J_{i,i+8} = J_{i+8,i} = -1$ (delay 1, 2, 3)
Number of ground states	2	2	16
Example of ground states $\{\sigma_i\}$	$\{1, 1, 1, 1, 1, 1, 1, 1, 1, 1, 1, 1, 1, 1, 1, 1\}$	$\{1, -1, 1, -1, 1, -1, 1, -1, 1, -1, 1, -1, 1, -1, 1, -1\}$	$\{1, -1, 1, -1, 1, -1, 1, -1, -1, 1, -1, 1, -1, 1, -1, 1, -1, 1\}$
Number of local minima	0	0	34
Ground state energy	-16	-16	-20
Average pumping power	1.00 W	900 mW	1.00 W
Experimental performance	1000/1000	996/1000	2000/2000
Simulation 1 (single-mode, 10000 round trips)	604/1000	588/1000	1000/1000
Simulation 2 (multimode, 200 round trips)	1000/1000	1000/1000	1000/1000

will grow at different rates, the ferromagnetic mode growing fastest. This lasts for a time T , which is logarithmic in the saturation power and inversely proportional to the normalized pump amplitude.

In the *saturation stage*, the field saturates to one of two values: $a \rightarrow \pm a_0$. The sign depends on the sign of the field after the growth stage. Different regions will have different signs, called *domains* in analogy to the classical ferromagnet, and these domains will be separated by topological defects (domain walls). The density of domain walls is a measure of the effective “temperature” of the system, with a larger density corresponding to a state of higher energy.

2.6.1 Growth stage

In the growth stage, the field $a_i(t)$ follows Eq.(16). Restricting attention to the 1D chain using a single delay line, this becomes:

$$\frac{da_i}{dt} = \frac{\log(G_0)}{2}(p-1)a_i + r^2(a_{i-1} - a_i). \quad (19)$$

The linear equation (Eq.(19)) is diagonalized by going to the Fourier domain $a_i \rightarrow \tilde{a}_k$. For small k , the result is:

$$\tilde{a}_k(T) = \underbrace{G_0^{\frac{1}{2}(p-1)T} e^{-2t^2 r^2 (\pi k/N)^2 T}}_{\text{gain}} \underbrace{e^{ik(2\pi r^2/N)T}}_{\text{drift}} \tilde{a}_k(0). \quad (20)$$

The two effects: gain and drift, are separated in Eq.(20). Drift is a result of the unidirectional coupling in Eq.(19). For a single delay line, the drift speed is $v_d = r^2$ [12] (with bidirectional coupling, e.g. [5, 11] this term disappears). The gain term depends on k , so different modes are amplified at different rates. This amplification stops when the fields reach their saturation value. If N_{sat} is the photon number at saturation and we start from vacuum noise, it takes approximately $\log(N_{\text{sat}})/\log(G/G_0)$ round trips to reach saturation, that is:

$$T = \frac{1}{p-1} \frac{\log(N_{\text{sat}})}{\log(G_0)}. \quad (21)$$

The logarithmic dependence of T on N_{sat} , which is $O(10^5 - 10^7)$ in fiber OPOs, means factors of two or three are not significant, so we can estimate $N_{\text{sat}} \rightarrow b_0^2$, the pump energy at threshold.

Starting with vacuum and propagating the growth equation Eq.(20) T time steps, we find that at the end of the growth stage the Fourier modes will be distributed as follows:

$$\tilde{a}_k(T) \sim \sqrt{N_{\text{sat}}} e^{-2r^2 t^2 T (\pi k/N)^2}. \quad (22)$$

The modes with smaller k have larger amplitudes, suggesting that the nearest-neighbor interaction forms some kind of short-range order. A good measure of this is the autocorrelation function $R(x)$. Before saturation, $R(x)$ is also a Gaussian:

$$R(x) \sim \langle a_i a_{i+x} \rangle = \sum_k e^{2\pi i k x / N} \langle \tilde{a}_k^* \tilde{a}_k \rangle \sim e^{-x^2 / 2x_0^2}, \quad (23)$$

where the correlation length at saturation is

$$x_0 \equiv \sqrt{2T} r t. \quad (24)$$

2.6.2 Saturation stage

In the next stage, pump depletion sets in and the fields inside the OPOs saturate. The simplest way to model this is to assume that the interaction term J_{ij} is negligible at this stage. Under this *simple saturation assumption* (SSA), the field in each OPO grows independently until it reaches one of two saturation values: $\pm\sqrt{(p-1)/\beta}$. The *sign* of the initial field $c_i(T)$ is preserved, and all its amplitude information is lost. This can be achieved with a sign function:

$$a_i(\infty) \approx a_{\text{sat}} \text{sign}[a_i(T)]. \quad (25)$$

Rather than collapsing into a single ferromagnetic state, the system forms domains of fixed spin, separated by fixed domain walls. This can be seen in the center plot of Fig. 10.

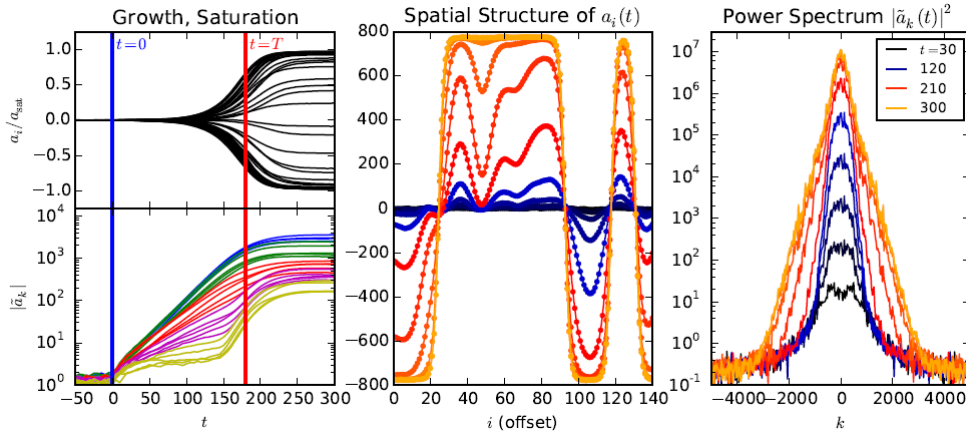


FIG. 10: Left: growth of OPO pulse amplitudes a_i (top) and Fourier modes \tilde{a}_k (bottom). Center: fields $a_i(t)$ for 1D chain at times $t = 30, 60, \dots, 300$ (x -axis shifted to cancel drift term). Right: power spectrum $|\tilde{a}_k|^2$ at times $t = 30, 60, \dots, 300$. Parameters: $G_0 = 7$ dB, $b/b_0 = 1.05$ [7].

However, Fig. 10 also reveals that the domain walls are not necessarily abrupt phase jumps as Eq.(25) would have. Depending on the coupling and pump strength, domain

walls can be quite wide. Near threshold, the shape admits an analytic solution via Eq.(19). Replacing the index i of $a_i(t)$ with a continuous variable, and rescaling the variables, one finds the equation:

$$\frac{\partial \bar{a}}{\partial \bar{t}} = (1 - \bar{a}^2)\bar{a} + \frac{1}{2} \frac{\partial^2 \bar{a}}{\partial \bar{x}^2} \quad (26)$$

$$(\bar{a} = a_0^{-1}a, \quad \bar{x} = (x - vt)/\ell, \quad \bar{t} = t/\tau) \quad , \quad (27)$$

where

$$a_0 = 2b_0 \sqrt{\frac{(b/b_0 - 1) \log G_0}{G_0 - (1 + \log G_0)}}, \quad \ell = \sqrt{\frac{2r^2(1 - r^2)}{(b/b_0 - 1) \log G_0}}, \quad v = r^2, \quad \tau = \frac{2}{(b/b_0 - 1) \log G_0}, \quad (28)$$

are the saturation field, domain wall length, drift speed, and relaxation time, respectively. Eq.(26) has an analytic solution: $\bar{a} = \pm \tanh(\bar{x} - \bar{x}_w)$. This is the domain wall.

The left plot of Fig. 11 zooms in on a domain wall. As the pump grows, the wall gets sharper, its width decreasing as $(b/b_0 - 1)^{-1/2}$ given in (Eq.(28)). If the pump is very strong or the coupling is weak, $\ell \lesssim 1$ and the smoothly-varying field assumption behind (Eq.(26)) breaks down. However, it seems to hold quite well for the values chosen here (the solid lines in the figure are the tanh solution).

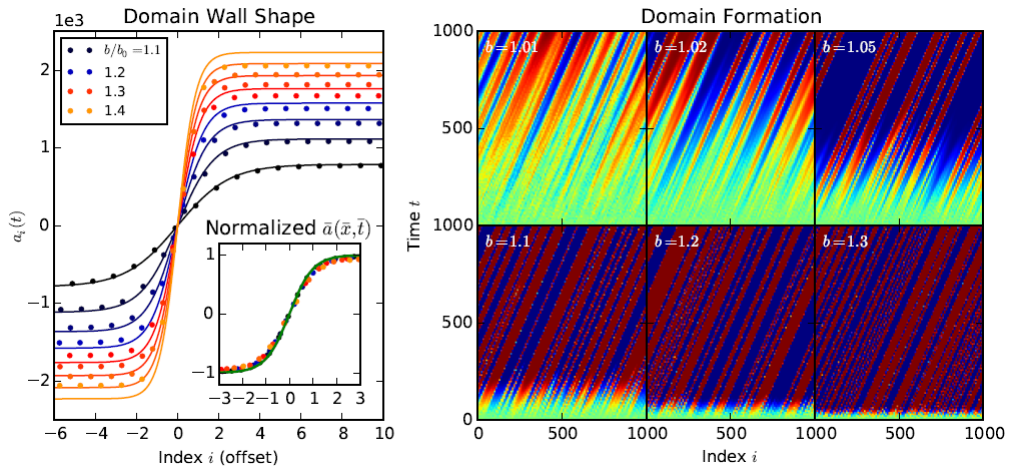


FIG. 11: Pulse amplitudes $a_i(t)$ near a domain wall as pump is swept slowly from $b/b_0 = 1.0$ to 1.4 (normalized units in inset). Right: color plot of pulse amplitudes $a_i(t)$ as function of index i (horizontal) and time t (vertical). Pump values b/b_0 range from 1.01 to 1.30 [7].

Domain walls are dynamic objects. In the presence of a perturbation, they move. Performing perturbation analysis about the tanh solution, one finds that the Hessian is singular:

most of its eigenvalues are $O(1)$ or larger, but for the vector $\partial a/\partial x$, it is zero. While other perturbations are strongly confined, perturbations along the $\partial a/\partial x$ direction are unimpeded. These correspond to moving the domain wall left or right. We can deduce the *domain-wall velocity* by taking the inner product (the eigenvalues are orthogonal):

$$\bar{v}_w = - \left[\int \frac{\partial \bar{a}}{\partial \bar{x}} \frac{\partial \bar{a}}{\partial \bar{x}} d\bar{x} \right]^{-1} \int \frac{\partial \bar{a}}{\partial \bar{t}} \frac{\partial \bar{a}}{\partial \bar{x}} d\bar{x} = -\frac{3}{4} \int \text{sech}^2(\bar{x} - \bar{x}_w) \frac{\partial \bar{a}}{\partial \bar{t}} d\bar{x}. \quad (29)$$

Consider a function $\bar{a}(x, t)$ with two domain walls at $\pm \bar{L}/2$. The precise way they are “glued together” at $\bar{x} \approx 0$ only matters to second order in the perturbation theory; $a = \tanh(\bar{L}/2 - |\bar{x}|)$ is a valid solution. Applying Eq.(29), one finds the following domain-wall speed and collision time:

$$\bar{v}_w = \frac{3}{2} \text{sech}^4(\bar{L}/2), \quad \bar{T}_{\bar{L}} = \frac{1}{48} e^{2\bar{L}}. \quad (30)$$

As the domain walls move, smaller domains will evaporate while large domains remain unaffected. All the domains that survive after a time t have a size $\bar{L} \geq (1/2) \log(48t)$.

The right plot in Fig. 11 shows the formation of domain walls as a color plot in both the pulse index i and time t . The domain drift is obvious here. In addition, the average domain size clearly shrinks the further the system is from threshold. Looking closely, one also sees events where domain walls collide and annihilate some of the smaller domains -- but in general this is rare, because the domains that form by time T tend to be moderate in size, and the lifetime (Eq.(30)) can be quite long.

2.7 Correlation length and defect density

The *computational performance* of the Ising machine is a measure of how well the final-state ($t \rightarrow \infty$) solution matches the exact ground state. As explained above, for finite-time calculations, the machine is not always in the desired ground state; often it finds a low-lying excited state with a small number of domain walls. The following statistics give a good measure of the computational performance:

1. Ground-state probability P . This decreases exponentially with chain size, but also increases with time to saturation.

2. Autocorrelation function $R(x) = \langle a_i a_{i+x} \rangle$. Both the CIM and thermal-equilibrium Ising models give an autocorrelation that is roughly exponential e^{-x/x'_0} , and the autocorrelation length x'_0 becomes the figure of merit. A perfect Ising solver will have $x'_0 \gg N$ (number of spins).
3. Defect density n_d , which is proportional to the average number of domain walls in the Ising chain. A perfect Ising solver will have $n_d \ll 1$.

The autocorrelation function, given by $R(x) = \langle a_i a_{i+x} \rangle / \langle a_i^2 \rangle$, takes the form $R(x) = \tanh(\beta J)^x$ for the thermal Ising model defined by $H = -\frac{1}{2}J \sum_i \sigma_i \sigma_{i+1}$. We can write this as e^{-x/x'_0} , with the correlation length $x'_0 = -\log(\tanh(\beta J))^{-1}$. Naturally, this length diverges at zero temperature. Since the Ising machine is not in thermal equilibrium, we do not expect *a priori* that $R(x)$ will be exponential. The easiest way to compute $R(x)$ as $t \rightarrow \infty$ is to assume the simple saturation approximation (Eq.(25)). Replacing $a_i(\infty) \rightarrow \text{sign}(a_i(T))$, the final-state autocorrelation is:

$$R(x; \infty) = 1 - 2P(a_i(T)a_{i+x}(T) < 0) = 1 - \frac{4}{\pi} \tan^{-1} \sqrt{\tanh(x^2/4x_0^2)}, \quad (31)$$

where T is the saturation time and $x_0 = \sqrt{2T} rt$ as in Eq.(24).

To compute $R(x)$ from the experimental data, one first reconstructs the pulse amplitudes $a_i(t)$ from the measurement record (Fig. 12, left). In Inagaki et al.[12], no local oscillator is present, so the signal is passed through a Mach-Zehnder with a one-bit delay line, measuring the quantities $I_{\pm,i} = |a_i \pm a_{i+1}|^2$. If the pulse energy $|a_i|^2$ is the same for each pulse, the angle between neighboring pulses is given by $\cos(\Delta\theta_i) = (I_{+,i} - I_{-,i}) / (I_{+,i} + I_{-,i})$. A negative value of $\cos(\Delta\theta_i)$ indicates a phase flip. Reconstructing a_i from these data, we then compute the autocorrelation length as a function of pump amplitude, obtained by fitting experimental data to (Eq.(31)). The experimental x_0 agree with Eq.(24), with a particular fit for $p = b/b_0 \approx 1.4$ shown in the inset. The exact function (Eq.(31)) is not quite exponential, but well-approximated by $R(x) \approx e^{-x/x'_0}$, with $x'_0 = 1.00463x_0$. Thus, we can obtain x_0 from experimental data by fitting the autocorrelation to an exponential. The relation $x_0 = \sqrt{2T} rt$ from the simple saturation approximation is quite good.

Another key statistic is the *defect (domain wall) density*. This is the average number of domain walls divided by the size of the chain $n_d = N_d/N$. The average domain length is then $L_d = 1/n_d$. For a thermal Ising model with $H = -\frac{1}{2}J \sum_i \sigma_i \sigma_{i+1}$, one has $n_d = (1 + e^{\beta J})^{-1}$.

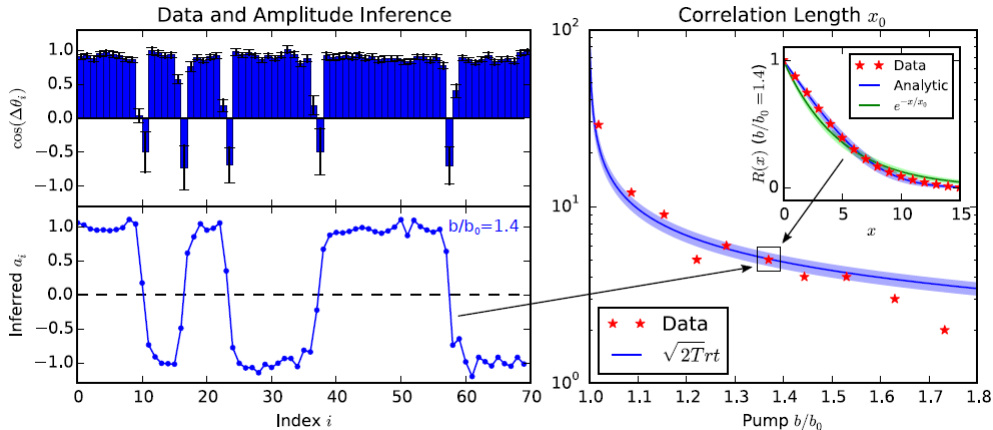


FIG. 12: Left: fiber OPO data for $\cos(\Delta\theta_i)$ (top) and reconstructed amplitude a_i (bottom). Right: autocorrelation length as a function of pump b/b_0 , compared to Eq.(24). Inset: autocorrelation $R(x)$ and analytic fits: form (31) in blue, exponential in green. Red stars are experimental data. Shaded regions show sensitivity of the analytic curves to N_{sat} when varied from 4×10^5 to 4×10^7 [7, 12].

TABLE II: Comparison of thermal Ising model and the coherent Ising machine [7].

	Thermal	CIM
Mechanism	Thermally-activated flips create a Boltzmann distribution.	Linear growth of OPO amplitudes, followed by saturation.
Correlation $R(x)$	e^{-x/x_0}	See Eq.(31)
Corr. length x_0	$-1/\log(\tanh(BJ/2))$	$\sqrt{2T}rt$
Defects n_d	$1/(1 + e^{BJ})$	$1/\pi x_0$
Success P_s	$\text{sech}(Ne^{-BJ})$	See Fig. 11

Since $a_i(\infty)$ has fixed amplitude, one can compute n_d from the autocorrelation function using the simple-saturation approximation: $n_d = (1 - R(1))/2$; for $x_0 \gtrsim 10$ $R(x)$ may be linearized about $x = 0$, giving the result:

$$n_d = \frac{1}{\pi x_0}, \quad L_d = \pi x_0, \quad x_0 = \sqrt{2T} rt. \quad (32)$$

Figure 13 (left) compares experimental data from Inagaki et al.[12][Fig. 4] to both Eq.(32) and numerical simulations. The fact that the data match the simulations when $t \rightarrow \infty$, but deviate from Eq.(32), suggests that the full numerical model works well, and domain-wall collision dynamics in the saturation stage improve the Ising machine performance relative to the simple saturation assumption (Eq.(25)).

The success probability P_s of the Ising machine is defined as the probability that it reaches the ground state at some time $T_{\text{final}} \gg T$. Figure 13 (right) plots the success probability

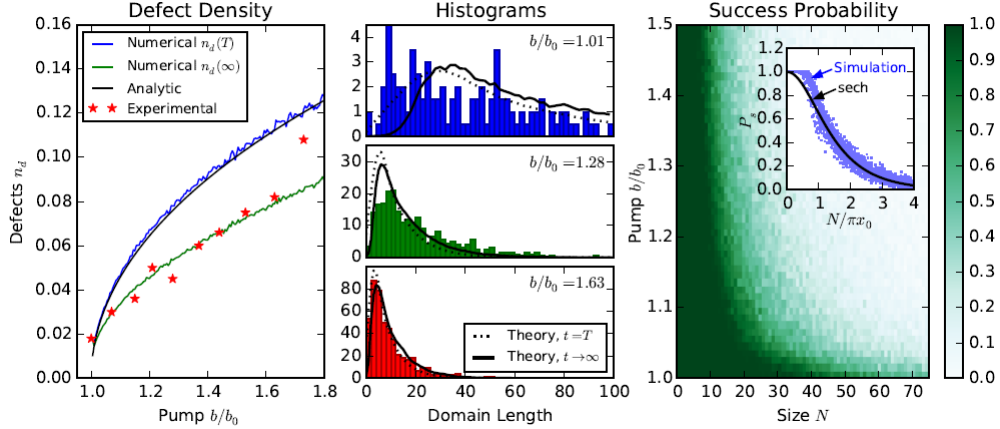


FIG. 13: Left: plot of defect density as a function of pump b/b_0 , numerical and analytic models (Eq.(32)) compared to experimental data. Center: domain length histograms for $b/b_0 = 1.01$, 1.28 and 1.63 . Bars denote experimental data. Right: success probability P_s as a function of system size N and pump b/b_0 [7, 12].

(numerically computed for $t \rightarrow \infty$) as a function of system size and pump power. As expected, the probability is greatest near threshold for small systems, where the average defect number $N/\pi x_0$ is small. Note that it roughly follows the line $P_s = \text{sech}(N/\pi x_0)$, which can be derived from a thermal model with defect density $N/\pi x_0$. This suggests that, for fixed x_0 , the success probability will fall exponentially with problem size N ; however, by increasing the time to saturation (gradual pumping), we can increase x_0 and thus reach the ground state in polynomial (quadratic) time in N .

Finally, the performance of the thermal Ising machine and the CIM are compared in Table II.

2.8 Multimode tunneling

2.8.1 Equations for signal fields and Hermite function expansion

The time-division multiplexed degenerate optical parametric oscillators (DOPOs) sometimes exhibit higher order pulse formation due to a large number of longitudinal cavity modes. We review the formulation according to the Ref. [13]. The signal field operator at the position $z \in [0, L)$ inside the cavity of its length L can be written as

$$\hat{E}_s(z, t) = \sum_m i\mathcal{E}\hat{s}_m(t)e^{i\omega_{s,m}(z/\nu - t)} + \text{H.c.}, \quad (33)$$

where \mathcal{E} is the single photon field amplitude and $\hat{s}_m(t)$ is the signal annihilation operator. The signal frequency of m -th longitudinal mode $\omega_{s,m} = \omega_0 + m\Omega$ ($m \in \mathbb{Z}$) has an interval of the cavity free spectral range Ω centered at ω_0 . After the pump adiabatic elimination, the signal annihilation operator obeys the following equation:

$$\begin{aligned} \frac{d\hat{s}_m}{dt} = & -\gamma_s \hat{s}_m - i(\Delta + m\Delta\Omega) + \sqrt{2\gamma_s} \hat{s}_{\text{in},m} \\ & + K \sum_q f_{m,q} \hat{s}_q^\dagger \hat{p}_{\text{in},m+q} - \frac{K^2}{4} \sum_{q,n} f_{m,q} f_{n,m+q-n} \hat{s}_q^\dagger \hat{s}_n \hat{s}_{m+q-n}. \end{aligned} \quad (34)$$

Here, the signal photon decay rate γ_s is equal to $\Omega T_s/4\pi$ with the transmittance (cavity loss) $T_s \ll 1$, the second term of the right hand side is the detuning Δ and pump timing mismatch $m\Delta\Omega$, and the coupling constant κ is included in $K = 2\kappa\sqrt{L/c}$. The phase-mismatching factor $f_{m,q}$ between two signal modes $m, q \in \mathbb{Z}$ is a sinc function of the phase-mismatch angle.

The parametric coupling between two signal modes is given by a matrix $\mathcal{L}_{m,q} = f_{m,q}\alpha_{m+q}$ composed of the phase-mismatching factor $f_{m,q}$ and the complex spectral component α_m . At the continuous limit, the component of its eigen vectors ψ_k are written by Hermite function

$$\psi_{k,m} = \frac{1}{\sqrt{k!2^k\sqrt{\pi}N_s}} e^{-\frac{1}{2}(\frac{m}{N_s})^2} H_k\left(\frac{m}{N_s}\right), \quad (35)$$

with an Hermite polynomial of order k and the number of signal modes $N_s = (\Omega\tau_s)^{-1}$.

Now the signal photon annihilation operators can be expanded by Hermite functions, $\hat{s}_m = \sum_{k \in \mathbb{N}} \psi_{k,m} \hat{S}_k$, and follow equations below by this basis transformation:

$$\begin{aligned} \frac{d\hat{S}_i}{dt} = & -(\gamma_s + i\Delta)\hat{S}_i + \sqrt{2\gamma_s} \hat{S}_{\text{in},i} \\ & - i\Delta\Omega \sum_{j,m} m \psi_{i,m}^* \psi_{j,m} \hat{S}_j + K \sum_{j,m,q} f_{m,q-m} p_{\text{in},q} \psi_{i,m}^* \psi_{j,q-m}^* \hat{S}_j^\dagger \\ & - \frac{K^2}{4} \sum_{j,k,l,m,q,n} f_{m,q-m} f_{n,q-n} \psi_{i,m}^* \psi_{j,q-m}^* \psi_{k,n} \psi_{l,q-n} \hat{S}_j^\dagger \hat{S}_k \hat{S}_l \end{aligned} \quad (36)$$

$$\begin{aligned} = & : -(\gamma_s + i\Delta)\hat{S}_i + \sqrt{2\gamma_s} \hat{S}_{\text{in},i} \\ & - i\Delta\Omega \sum_j D_{ij} \hat{S}_j + K \sum_j G_{ij}(p_{\text{in}}) \hat{S}_j^\dagger - \frac{K^2}{4} \sum_{j,k,l} L_{ijkl} \hat{S}_j^\dagger \hat{S}_k \hat{S}_l, \end{aligned} \quad (37)$$

where D_{ij} and G_{ij} denote coefficient for pump timing mismatch and PPLN OPA gain,

respectively, while L_{ijkl} denotes signal mode coupling between two coupled modes (i, j) and (k, l) . In a coherent Ising machine, N DOPOs are mutually coupled each other with given coupling constants [14]. The set of Eq. (37) including the mutual coupling term is used in the numerical simulation.

2.8.2 Dynamics of the multimode tunneling

Here, we show the picture of the multimode tunneling in DOPOs with Fig. 14(a). In the system of single-mode DOPOs, the phase flip of a macroscopic oscillator field requires to pass through the complete cancellation of the mode (the state with zero amplitude), which is unfavorable. On the other hand, a multimode DOPO can switch between the binary phase states by rotating its phase with the excitation of higher spatio-temporal modes which have different frequencies. It helps the system escape from unstable states and smoothly find a ground state of the programmed Ising model. Fig. 14(b) displays an example of simulated dynamics of the phase flip in a multimode DOPO pulse under mutual injections aligned in the one-dimensional ring, with a uniform amplitude coupling coefficient $\xi = 0.008$. When the sign of the fundamental mode amplitude s_0 is reversed, those for higher modes temporarily rise and keep the intensity of the whole pulse. Such a transition enhances the tunneling rate of a multimode DOPO compared to a single mode system. More details will be published elsewhere [15].

2.8.3 Simulated performance

The performance of 16-pulse DOPO Ising machine is numerically evaluated. Here, both the single-mode and multimode treatments of in-phase signals are calculated by fourth-order Runge-Kutta method. Note that the effective number of signal modes in multimode simulation (indexed by k in Eq. (35)) is assumed to be 5 for each pulse. A stepwise and constant pumping rate of $1.1 I_{th}$ is introduced at $t = 0$, with I_{th} being the oscillation threshold for the single DOPO. The phase states of the fields are read out after 200 times the cavity lifetime for a single run, and then 1000 trials are used to estimate the success probability. The result, when the coupling constant is 7.5%, is summarized in Table III. The Ising problems are performed on three graphs as in the experimental demonstration:

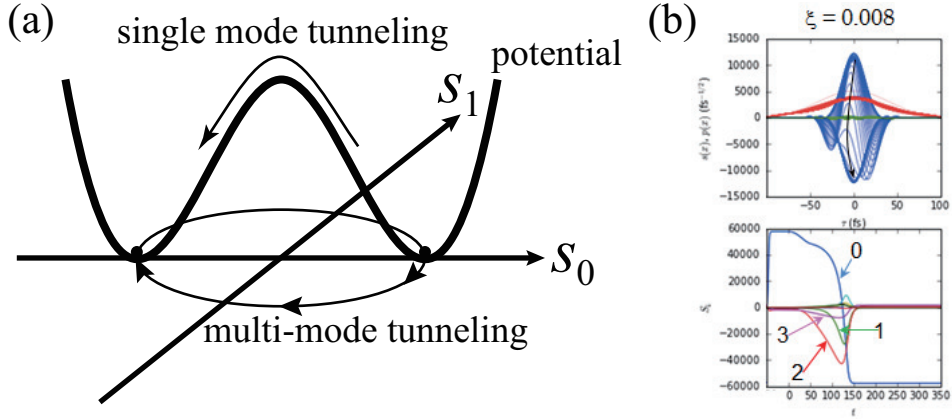


FIG. 14: (a) Schematic and (b) Simulated dynamics of the phase flip in a multimode DOPO. Upper panel in (b): temporal profiles of Hermite modes of a DOPO pulse. Lower panel: time evolution of the coefficients of the modes [11].

the ferromagnetic one-dimensional ring, the anti-ferromagnetic one-dimensional ring, and an anti-ferromagnetic cubic graph. The difference between single-mode and multimode is significant in two (ferromagnetic and anti-ferromagnetic) one-dimensional rings, while the ground states of the cubic graph with $N = 16$ is 100% attainable in both methods. We add the result for the cubic graph with $N = 4$, which was experimentally solved in the previous study [5].

TABLE III: Success rate in 1000 trials of numerical calculations for Ising problem on three graphs of order $N = 16$ [11].

	ferro	anti-ferro	cubic ($N = 16$)	cubic ($N = 4$)
single-mode	.593	.599	1.000	.930
multimode	1.000	1.000	1.000	1.000

2.9 XY machine based on nondegenerate OPO

In statistical physics, the XY model refers to a network of spins $\vec{\sigma}_i \in \mathcal{R}^2$, $|\vec{\sigma}_i|^2 = 1$, with the Hamiltonian $U(\sigma) = -\frac{1}{2} \sum_{ij} J_{ij} \vec{\sigma}_i \cdot \vec{\sigma}_j$. Each spin has a continuous $U(1)$ degree of freedom, rather than being discrete-valued. It could equivalently be formulated in terms of angles, with $\vec{\sigma}_i = (\cos \phi_i, \sin \phi_i)$ living in a potential

Thus the nondegenerate OPO has a ring of steady states, each with its own phase. The spin $\vec{\sigma}_i$ is represented with this phase.

Solving the equations of motion follows the same lines as in Sec.1. The general three-wave mixing problems can be solved analytically in terms of Jacobi elliptic functions [1], but a simple form is possible if we assume that $ab \in \mathbb{R}$, since this is the mode that experiences gain, while the imaginary part experiences loss. We can then solve for the absolute values of the fields,

$$\frac{d|\bar{a}|}{ds} = \epsilon|\bar{b}|\bar{c}, \quad \frac{d|\bar{b}|}{ds} = \epsilon|\bar{a}|\bar{c}, \quad \frac{d\bar{c}}{ds} = -\epsilon|\bar{a}||\bar{b}|, \quad (42)$$

which can be integrated exactly, along the lines of Sec.1.

Since the OPO state is defined by two fields (a, b) now, there are two possibilities: singly-resonant (where only the signal resonates) and doubly-resonant (where both signal and idler resonate). We will consider the doubly-resonant case here (but the singly-resonant case, discussed in [7], is similar). If the signal and idler frequencies are similar enough and we don't filter one of them out, we have a doubly-resonant system and they will propagate through the cavity with the same Q factor. As a result, a and b will have the same magnitude. If, furthermore, the overall phase is stabilized, then we have $a = b^*$. All modes orthogonal to the $a = b^*$ subspace experience loss in the gain medium, and can be ignored.

Setting $b_{\text{in}} = a_{\text{in}}^*$, Eq.(42) reduce to $da/dz = \epsilon a \sqrt{c_{\text{in}}^2 + a_{\text{in}}^2 - a^2}$. This gives an input-output relation that matches Eq.(6) up to scaling factors:

$$a_{\text{out}} = a_{\text{in}} G_0^{\frac{1}{2} \sqrt{a_{\text{in}}^2 + c_{\text{in}}^2} / c_0} \left[1 + (G_0^{\sqrt{a_{\text{in}}^2 + c_{\text{in}}^2} / c_0} - 1) \frac{1 - \sqrt{1 - (a_{\text{in}} / \sqrt{a_{\text{in}}^2 + c_{\text{in}}^2})^2}}{2} \right]^{-1}. \quad (43)$$

Linearizing (Eq.(43)) for small input fields, we find $a_{\text{out}} = G_0^{c/2c_0} a_{\text{in}}$. Thus the (power) gain for the nonlinear waveguide pumped above threshold is the same as in the degenerate case: $G = G_0^{c/c_0}$. Going to third order in a_{in} , it is not hard to derive the XY version of Eq.(7), valid when the pump is near threshold:

$$a_{\text{out}} = a_{\text{in}} \sqrt{G/G_0} \left[1 - \frac{G - (1 + \log G)}{4} \frac{|a_{\text{in}}|^2}{c^2} + O((a_{\text{in}}/b)^4) \right]. \quad (44)$$

As in the degenerate case, quantum noise can be modeled by adding vacuum fluctuations to the input pump field $c_{i,\text{in}} \rightarrow c_{i,\text{in}} + w_i^{(c)}$ and treating signal / idler loss as a lumped element after the gain medium: $a_{i,\text{out}} \rightarrow a_{i,\text{out}} + \sqrt{1 - 1/G_0} w_i^{(a)}$ (plus $b_{i,\text{out}} \rightarrow b_{i,\text{out}} + \sqrt{1 - 1/G_0} w_i^{(b)}$ if doubly resonant). Here, w is a discrete-time noise process with vacuum statistics: $\langle w^* w \rangle = \frac{1}{2}$.

Optical coupling can be introduced using delay lines, as shown in Fig. 5. Tracing the paths in the canonical delay-line diagram (Fig. 5), vacuum enters the cavity through the first beamsplitter. The transmitted beam passes along the cavity without delay, while the reflected beam is delayed by one pulse spacing, contributing to a_{i+d} instead. There are five parameters: r, t, r', t', ϕ , which can in principle vary in time.

$$a_i \rightarrow t_i t'_i a_i + r_i r'_{i-d} e^{i\phi_i} a_{i-d} + \left(t_i r_i w_i^{(J)} + r_i t_{i-d} e^{i\phi} w_{i-d}^{(J)} \right). \quad (45)$$

Couplings will be more difficult to implement in the doubly-resonant regime because both signal and idler fields propagate with separate parameters r, t, r', t', ϕ . To maintain the condition $a = b^*$ the beamsplitter coefficients must be the same and the phases must be opposite:

$$\begin{aligned} a_i &\rightarrow t_i t'_i a_i + r_i r'_{i-d} e^{i\phi_i} a_{i-d} + \left(t_i r_i w_i^{(J,a)} + r_i t_{i-d} e^{i\phi} w_{i-d}^{(J,a)} \right) \\ b_i &\rightarrow t_i t'_i b_i + r_i r'_{i-d} e^{-i\phi_i} b_{i-d} + \left(t_i r_i w_i^{(J,b)} + r_i t_{i-d} e^{-i\phi} w_{i-d}^{(J,b)} \right). \end{aligned} \quad (46)$$

Dynamics of the XY machine closely parallel the Ising machine. The computation process is divided into two stages: a linear *growth stage*, where the signal and idler grow subject to the linear coupling term; and a nonlinear *saturation stage* where the amplitude saturates. With the amplitudes saturated out, the remaining dynamical variables are the phases $\phi_i = \arg(a_i)$. In this stage, the system evolves according to the Kuramoto model

$$\frac{d\phi_i}{dt} \propto - \sum_j J_{ij} \sin(\phi_i - \phi_j) = - \frac{\partial U}{\partial \phi_i}, \quad (47)$$

where U is the Kuramoto potential given in Eq.(38). Thus the saturation stage is also called the *Kuramoto stage*.

2.9.2 1D chain

A ferromagnetic 1D chain is realized with a single delay line of phase 0; see Sec. 6. The linear dynamics of $a_i(t)$ are the same as for the Ising model: working in the Fourier basis $\tilde{a}_k(t)$, the system of difference equations diagonalizes. The initial quantum noise is amplified to macroscopic values. At the saturation time $T = (c/c_0 - 1)^{-1} \log(N_{\text{sat}})/\log(G_0)$, these Fourier modes have mean amplitude:

$$\sqrt{\langle |\tilde{a}_k(T)|^2 \rangle} = \sqrt{N_{\text{sat}}} e^{-2r^2 t^2 T (\pi k/N)^2}. \quad (48)$$

The dominant Fourier mode is the zero mode (the XY ground state for the 1D problem), and higher Fourier modes are suppressed by the exponential $e^{-2r^2 t^2 T (\pi k/N)^2}$. At saturation, the state has a correlation length $x_0 = \sqrt{2T} rt$. The key difference from the degenerate case is that *both* quadratures of a_i experience gain in the XY model. After the growth stage, the amplitude a_i quickly saturates, but the phase is still free to move. Assuming $a_i(t) = a_{\text{sat}} e^{i\phi_i(t)}$, the phase is found to follow the difference equation:

$$\phi_i(t+1) = [t^2 \phi_i + r^2 \phi_{i-1}]. \quad (49)$$

Equation (49) is a linear equation with the boundary condition $\phi_N = \phi_0 + 2m\pi$. As in the growth stage, the best way to solve it is to use a Fourier series:

$$\phi_x = \frac{mx}{N} + \sum_k \phi_k e^{2\pi i k x/N}. \quad (50)$$

Note that Eqs.(49) and (50) are the same up to the constant gain term. Thus the eigenvalues for the ϕ_k will be:

$$\lambda_k = \frac{\phi_i(t+1)}{\phi_i(t)} = t^2 + r^2 e^{-2\pi i k/N} = \underbrace{e^{-\frac{1}{2}(rt)^2 (2\pi k/N)^2}}_{\text{diffusion}} \underbrace{e^{ir^2(2\pi k/N)}}_{\text{drift}}. \quad (51)$$

The steady state will be a state of constant winding $\phi_x = mx/N$. For $m = 0$ this is the global minimum for the XY potential, for $m \neq 0$ an excited local minimum. For sufficiently long chains, where $N \gg x_0$, the parts of the chain separated by $\gtrsim x_0$ are uncorrelated, so on these length-scales, the phase executes a random walk. Thus the average number of windings is normally distributed about zero, with a standard deviation that goes as

$\langle m^2 \rangle^{1/2} \approx 0.232 \sqrt{N/x_0}$ (the constant must be determined numerically), which is confirmed experimentally as shown in Fig. 16.

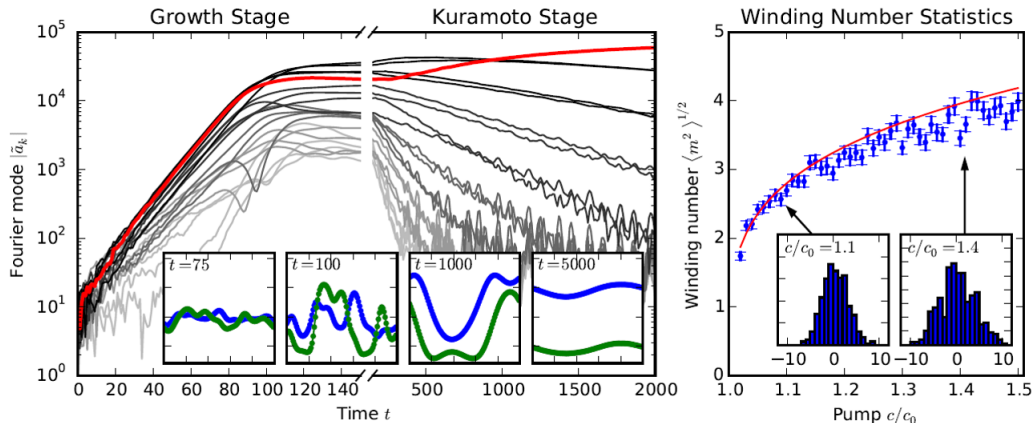


FIG. 16: Left: Fourier modes $|\tilde{a}_k(t)|$ for a 100-spin XY machine simulation. Right: average winding number $\langle m^2 \rangle^{1/2}$, with the fit $0.232 \sqrt{N/x_0}$ [7, 12].

Note the two timescales in this problem, as shown in Fig. 16. The first is the growth-stage time. If we want to reach the global minimum, the growth stage must be long enough for $x_0 \approx N$. Since $x_0 = \sqrt{2T}rt$, this constrains the growth-stage time to be $T \gtrsim (N/rt)^2$. On the other hand, just to reach a local minimum, we must wait long enough in the Kuramoto stage for the phase excitations ϕ_k to decay to zero -- this takes $O(N/rt)^2$ time as well. So no matter what kind of minimum we want, global or local, we must wait $O(N/rt)^2$ time, but to get the global minimum, this must happen in the growth stage, when the field is weak compared to saturation.

Another important thing to note is that the precise form of the nonlinear input-output map $a_{\text{in}} \rightarrow a_{\text{out}}$ does not matter. In the growth stage, this map is linearized so all that matters is the gain, which determines the saturation time. In the Kuramoto stage, since the amplitude saturates much more rapidly than the phase dynamics, the equation for ϕ_i does not even depend on the gain element. This seems to suggest that all XY machines are equivalent when it comes to solving the 1D Ising problem.

These theoretical predictions are fully confirmed in experiments by using a laser network [16] and nondegenerate OPO network [17] as XY machines.

2.9.3 2D lattice

As far as local minima are concerned, the 2D lattice is just like a 1D chain in two directions. The spins are indexed by two coordinates $a_{i,j}$ with the connections $a_{i,i} \rightarrow a_{i,i+1}$, $a_{i,i} \rightarrow a_{i+1,i}$ and the equilibrium solutions are states of constant winding number: $a_{x,y} = e^{i(m_x x + m_y y)}$. The growth stage is also analogous: the Fourier amplitudes grow according to Eq.(48) so that the autocorrelation is $e^{-(x^2+y^2)/2x_0^2}$.

Having saturated the amplitude and thus reached the Kuramoto stage, the 2D model becomes quite different. Topological *vortex defects* form and the dynamics are dominated by inter-vortex interactions, as shown in Fig.17.

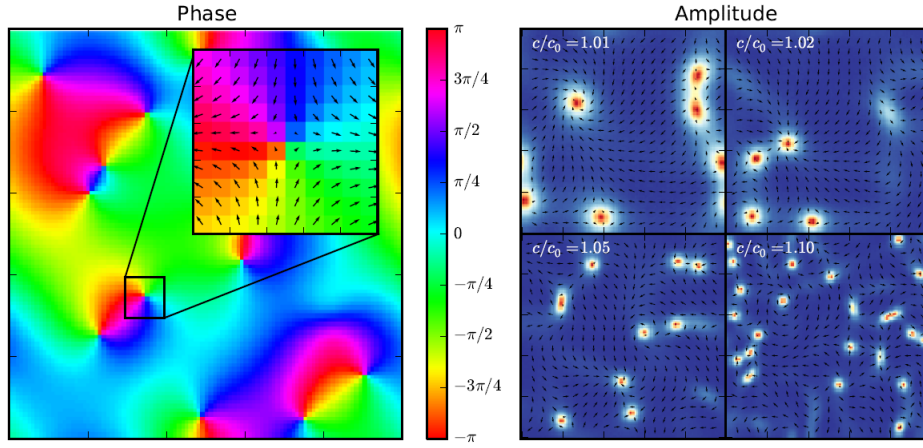


FIG. 17: Phase (left) and amplitude (right) for 2D XY model with vortices [7].

For an infinite lattice, an isolated vortex is a stable solution to the round-trip equations of the OPO. Following the analysis leading to Eq.(26), which is applicable in the near-threshold limit, the round-trip equations can be rewritten as a nonlinear PDE with gain and diffusion:

$$\frac{\partial a}{\partial t} = \left[\frac{\log G_0}{2} (c/c_0 - 1) - \frac{G_0 - (1 + \log G_0) |a|^2}{4 c_0^2} \right] a + \frac{r^2(1-r^2)}{2} \left[\frac{\partial^2 a}{\partial \xi_x^2} + \frac{\partial^2 a}{\partial \xi_y^2} \right], \quad (52)$$

where $\xi_x = x - r^2 t$, $\xi_y = y - r^2 t$. Scaling a, x, y, t one converts this to its canonical form:

$$\frac{\partial \bar{a}}{\partial \bar{t}} = (1 - |\bar{a}|^2) \bar{a} + \frac{1}{2} \left(\frac{\partial^2 \bar{a}}{\partial \bar{x}^2} + \frac{\partial^2 \bar{a}}{\partial \bar{y}^2} \right). \quad (53)$$

Going to polar coordinates (r, ϕ) , the vortex is the solution $A(r)e^{\pm i\phi}$ with $A(r)$ satisfying

the differential equation $\frac{1}{2}(A'' + r^{-1}A') + (1 - A^2 - 1/(2r^2))A = 0$. It turns out that $A(r) \approx \tanh(r)$ is a good approximation for the amplitude.

To calculate the number of vortices at time T , one finds the probability that the phase winds 2π around one unit cell of the lattice. This is a straightforward calculation in the growth stage, because the joint probability of any set of amplitudes a_i is always a Gaussian with covariances $\langle a_i a_j \rangle = e^{-1/2x_0^2}$ between neighboring points on any lattice cell $a_{\text{sq}} = [a_P, a_Q, a_R, a_S]$, and $\langle a_i a_j \rangle = e^{-1/x_0^2}$ for opposite points. A dimensional analysis shows that the vortex density must go as x_0^{-2} , with a constant given by [7]

$$n_v \equiv P(\text{vortex}|a_{\text{sq}}) \approx \frac{0.159}{x_0^2}. \quad (54)$$

The total number of vortices will be Nn_v , where N is the size of the lattice. Note that, consistent with our study of the 1D ring (for both Ising and XY machines), the defect density decreases with increasing x_0 , which scales with the time to saturation $x_0 \propto T^{1/2}$. Since the time to saturation is longer for systems closer to threshold, a slower anneal (pumping closer to threshold) leads to states with fewer vortex excitations, i.e. closer to the true ground state.

While a single vortex is stable, nearby vortices interact with each other. According to the classical Berezinskii-Kosterlitz-Thouless theory on vortices in XY models [18], the interaction is Hamiltonian and the motion is neither attractive or repulsive. By contrast, in the coherent XY machine, the interaction is dissipative and the motion (for oppositely charged vortices) is attractive.

Figure 18 illustrates the vortex interactions once the XY machine has reached the Kuramoto stage. For a complex field of arbitrary amplitude, one can define the vorticity as $\nabla a^* \times \nabla a$. The winding number around a loop (for which the field has constant amplitude) equals the integral of the vorticity inside the loop. This vorticity is plotted as a function of position and time, and the regions of nonzero vorticity correspond to regions where the phase wraps by 2π . Following the plots from left to right, one sees that vortices of opposite vorticity are attracted to each other and eventually annihilate, consistent with the vortex interaction picture sketched above.

The right plot shows the average number of vortices on a 100×100 XY model for pump amplitudes ranging from $c/c_0 = 1.01$ to 1.50 . In this plot, the “number of vortices” was

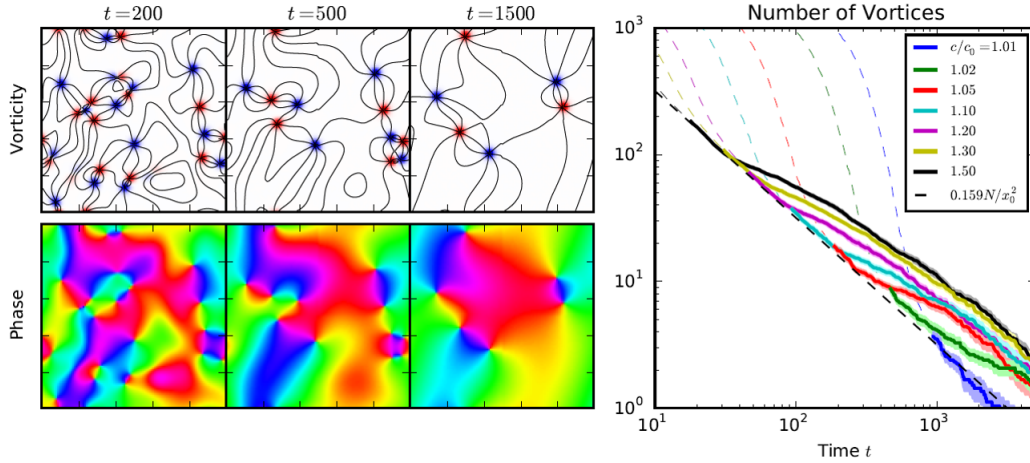


FIG. 18: Left: plots of vorticity and phase as a function of time (simulation used $c/c_0 = 1.1$). Right: vortex number as a function of time and pump power ($t > T_{\text{sat}}$ in bold) [7].

defined as the number of unit cells in which the phase winds by $\pm 2\pi$. Well below saturation, when the field amplitudes are random, the number of such “vortices” is very high. By the end of the growth stage, the vortex count stabilizes at $0.159N/x_0^2$, consistent with Eq.(54). Thereafter the system enters the Kuramoto stage and its dynamics are driven by vortex-vortex interactions.

-
- [1] J.A .Armstrong et al., Phys Rev. 127, 1918 (1962).
 - [2] R. W. Boyd, Nonlinear Optics. Academic Press (2003).
 - [3] C. M.Caves, Phys. Rev. D 23, 1963 (1981).
 - [4] E. Arthurs et al., Bell Syst. Tech. J. 44, 725 (1965).
 - [5] A. Marandi et al., Nature Photonics 8, 937 (2014).
 - [6] R. Hamerly et al., Phys. Rev. A 94, 063809 (2016).
 - [7] R. Hamerly et al., Int. J. Mod. Phys. B 30, 1630014 (2016).
 - [8] H. Goto, Sci. Rep. 6, 21686 (2016).
 - [9] S. Puri et al., Nat. Commun. 8, 15785 (2017).
 - [10] Y. Haribara et al., in Principles and Methods of Quantum Information Technologies, 251-262. Springer (2016).
 - [11] K. Takata, et al., Sci. Rep. 6, 34089 (2016).
 - [12] T. Inagaki et al., Nature Photonics 10, 415 (2016).

- [13] G. Patera et al., The European Physical Journal D 56, 123 (2010).
- [14] Z. Wang et al., Phys. Rev. A 88, 063853 (2013).
- [15] A. Marandi et al., in preparation.
- [16] S. Tamate et al., arXiv:1608.00358 (2016).
- [17] Y. Takeda et al., arXiv:1705.03611 (2017).
- [18] J. M. Kosterlitz et al., Journal of Physics C: Solid State Physics 6, 1181 (1973).

Written by R. Hamerly and Y. Yamamoto

version 1